

Mammotomography with Pinhole Incomplete Circular Orbit SPECT

Martin P. Tornai, PhD^{1,2}; James E. Bowsher, PhD¹; Ronald J. Jaszcak, PhD^{1,2}; Brett C. Pieper, MS^{1,2}; Kim L. Greer¹; Patricia H. Hardenbergh, MD³; and R. Edward Coleman, MD¹

¹Section of Nuclear Medicine, Department of Radiology, Duke University Medical Center, Durham, North Carolina; ²Department of Biomedical Engineering, Duke University, Durham, North Carolina; and ³Department of Radiation Oncology, Duke University Medical Center, Durham, North Carolina

Dedicated mammotomography with pinhole incomplete circular orbit (PICO) SPECT imaging of an uncompressed pendant breast was evaluated with small, very-high-stopping-power pinhole apertures. Comparisons were made with planar pinhole scintimammography. Enhanced 3-dimensional imaging performance with very-high-stopping-power apertures is thought to ultimately yield improved sensitivities for lesion detection and identification in breast disease. **Methods:** Pinhole collimators made of high-density and high atomic number ¹⁸⁴W or depleted ²³⁸U, with aperture diameters from 1 to 4 mm, were used to image 0.6- and 1.0-cm-diameter spherical lesions in a pendulous, uncompressed breast phantom in planar and PICO-SPECT modes. The breast was centered on the horizontal axis of rotation of an incomplete circular orbit. Lesion, breast and body, and myocardial activities (L:B:M) were included in the phantoms to simulate clinical imaging conditions with ^{99m}Tc (140 keV). Lesion contrasts and signal-to-noise ratios (SNRs) for all apertures were determined for near clinical acquisition times for L:B:M ratios of 12:1:20 and 7:1:25. A set of minidisks inserted in the breast phantom was scanned to determine sampling limitations at depth from the nipple. In an initial study, a patient with biopsy-confirmed breast carcinoma was injected with 960 MBq ^{99m}Tc-tetrofosmin and scanned 2 h later with planar pinhole and PICO-SPECT techniques. **Results:** Overall, for PICO-SPECT imaging there were small differences in measured counting rate sensitivity (4.9%) and lesion contrast (8.8%) with larger SNR differences (20.8%) between tungsten and depleted uranium pinhole materials at this energy and these lesion sizes. Backgrounds from simulated myocardial uptake had minor contributions in all reconstructed image volumes because of the rapid sensitivity fall-off for pinhole apertures. An optimal aperture diameter between 2 and 3 mm was determined from peak SNR, indicating that these aperture sizes may have the best performance for lesions as small as 0.6 cm in diameter with activity concentration ratios of ^{99m}Tc similar to those currently seen in patients. Both lesions were visualized with PICO-SPECT better than with planar pinhole imaging, with respective contrast improvements >20 times the values obtained from planar imaging for the same pinholes. In the patient study, higher contrast

(>6) visualization of the active tumor periphery was obtained with PICO-SPECT than with planar imaging. **Conclusion:** These results indicate that the enhanced spatial resolution of smaller apertures outweighs the loss in sensitivity in small lesion identification with PICO-SPECT. Although the imaging differences between investigated aperture types are small and some limitations to this imaging approach exist, dedicated PICO-SPECT of the breast appears to be an improved technique compared with conventional planar pinhole scintimammography. This technique provides enhanced contrast and SNR for imaging small lesions with the high-resolution pinhole apertures along with 3-dimensional localization of the lesions.

Key Words: SPECT; breast scintigraphy; scintimammography; pinhole incomplete circular orbit; mammotomography

J Nucl Med 2003; 44:583–593

The use of ^{99m}Tc-labeled compounds to detect malignant breast disease has spurred development of various approaches to radionuclide imaging of breast cancer (1–5). Conventional SPECT for breast disease is limited by the resolution degradation resulting from the large radius of rotation (ROR) required to rotate the camera system with horizontal axis of rotation (AOR) about the patient, attenuation of the breast signal through the torso, and primary and scatter contamination from other organs that accumulate the radiopharmaceutical. Results from clinical studies indicate that the benefits of conventional SPECT compared with planar scintimammography imaging for breast disease are still debatable (5–7), despite the fact that there should be higher contrast of deeply seated lesions with tomographic imaging (8). However, preliminary dedicated breast SPECT approaches using parallel, pinhole, and other collimator configurations have demonstrated that application-specific imaging of the breast can provide improved images of breast lesions (9–21).

Contemporary nuclear medicine techniques for imaging suspected breast cancer involve planar, parallel-hole collimated imaging of a pendulous breast hanging from the anterior chest wall of a patient lying prone. This orientation

Received May 2, 2002; revision accepted Sep. 25, 2002.

For correspondence or reprints contact: Martin P. Tornai, PhD, Department of Radiology, Duke University Medical Center, DUMC 3949, Durham, NC 27710.

E-mail: martin.tornai@duke.edu

decreases contamination from torso uptake of radiopharmaceutical and minimizes scatter. Two specific benefits are associated with pinhole collimation for breast lesion imaging: (a) the improved resolution and sensitivity characteristics of pinhole collimators compared with those of parallel-hole collimators at short RORs for SPECT and (b) the dramatic sensitivity fall-off for pinhole collimators with increasing distance from the collimator as compared with the uniform sensitivity of parallel-hole collimators and increasing sensitivity of convergent-hole collimators. The first point may facilitate smaller lesion visualization than is possible with current parallel-hole imaging techniques on clinical gamma cameras. The second point should ensure that torso background contamination plays a more minor role in dedicated breast lesion imaging. Planar pinhole breast imaging has been investigated and shown to provide improved lesion visualization results over conventional planar parallel-hole imaging (22). A recent study used a tuned-aperture pinhole collimator and demonstrated with Monte Carlo simulations and phantom measurements that this blurring tomography technique improves lesion contrast and signal-to-noise ratio (SNR) compared with planar pinhole imaging (23). The use of multiple pinholes has been proposed in an effort to increase sensitivity and, consequently, image quality (13).

In these experimental cases (9–12,15,16,20,23), dedicated tomographic breast imaging results were superior to planar imaging results, and overall imaging with pinhole collimators yielded superior performance for breast lesion visualization (10,22,23). Specifically, a dedicated, fully tomographic breast imaging approach described measurements with a developmental (rectangular, box-shaped) pinhole support system rotating about the pendant breast phantom in an incomplete circular orbit with the standard horizontal AOR of the SPECT scanner (10). A study with a tilted-head pinhole geometry shows promise for this application as well (24). In another example, a recent clinical application of pinhole imaging with an incomplete circular orbit to image axillae involved with breast cancer yielded higher contrast images than planar imaging and was successful in improving lesion sensitivity by 50% in patients (25).

In orbital trajectories similar to those of Gullberg and Zeng (26) for cardiac imaging, our pinhole collimated camera traverses 150° to approximately 180° (Fig. 1). Note that with pinhole (or cone beam) imaging confined to a single plane (a circular trajectory), the only completely sampled region is in the central plane. Our objective was to evaluate small, very-high-stopping-power pinholes with incomplete circular orbit (PICO) SPECT for dedicated breast imaging. One hypothesis is that this incomplete circular orbit SPECT technique should provide improved visualization of smaller lesions or lesions of lower activity uptake compared with scintimammography using the same pinhole collimators.

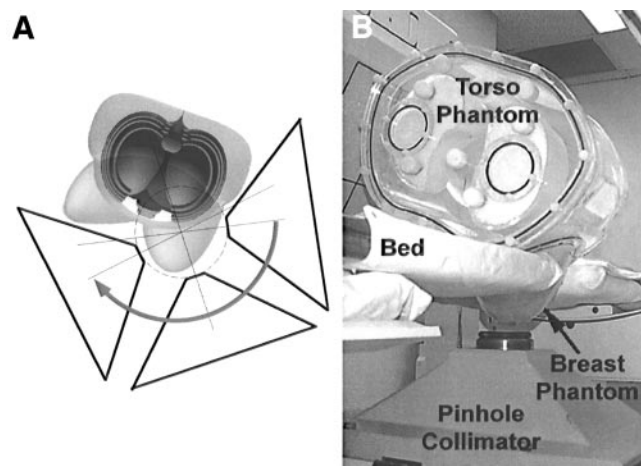


FIGURE 1. (A) Schematic near-scale diagram of 3 positions in <180° PICO-SPECT orbit about pendulous breast with pyramidal pinhole collimator. Detector is at large end of trapezoidal collimator housing with pinhole aperture centered at smaller end. Angular range is somewhat idealized, because contralateral breast would be compressed against specialized bed that provides hole for breast being imaged. (B) Photograph of anthropomorphic torso phantom with left breast attachment in specially designed bed, with pinhole collimator assembly on 1 camera head.

Another hypothesis is that ^{184}W apertures provide images comparable to images made with very-high-stopping-power pinhole apertures made of depleted ^{238}U (DU) for $^{99\text{m}}\text{Tc}$ compounds. Finer-resolution planar or tomographic images should result if penetration at the pinhole aperture edge is minimized or totally eliminated, and these 2 materials are both good candidates to determine this. Whereas penetration and scatter at the aperture edge may provide higher sensitivity with a given pinhole aperture (27) for lower-stopping-power materials, reduced resolution would result. Thus, high-resolution pinhole imaging with a fully tomographic approach for those lesions close to the pinhole aperture may ultimately result in improved sensitivities and specificities for lesion detection and identification.

The dedicated PICO-SPECT measurements in the current work were made by adapting a contemporary clinical SPECT system with a pinhole collimator to image lesions in a pendant breast. In an effort to evaluate, characterize, and improve this PICO-SPECT approach, we performed various measurements with novel pinhole inserts on a pyramidal pinhole-collimator system by imaging a breast containing lesions of various sizes and activity concentration ratios. Lesion contrast and SNRs were obtained from planar and PICO-SPECT measurements to determine trade-offs between collimator sensitivity and resolution and their impact on lesion visualization. Pinhole aperture diameters for maximizing lesion SNR for PICO-SPECT were determined, and lesion contrasts were characterized. Based on those results, initial patient planar and PICO-SPECT studies were performed with the near-optimal aperture for PICO-SPECT.

TABLE 1
Comparison of Some Characteristics of Pure Materials
Used in Pinhole Inserts (29)

Material	Atomic number	Density (g/cm ³)	μ_{total} (cm ⁻¹) at 140 keV
Lead	82	11.35	27.2
Tungsten	74	19.3*	36.4
Gold	79	19.32	42.7
Platinum	78	21.45	45.8
Iridium	77	22.41	46.4
Uranium	92	18.95	58.1

*Value is for pure tungsten, whereas alloy used in this work had density of 18.5 with fractional tungsten content of 0.97.

MATERIALS AND METHODS

A 3-head clinical gamma camera (Triad XLT-9; Trionix Corporation, Twinsburg, OH) with a 40-cm transverse \times 20-cm axial field of view (FOV) and 9-mm-thick NaI(Tl) scintillator, was used for all experiments. Image data were thus acquired in 128 \times 64 pixel matrices. The system allows for sufficient radial head retraction for patient PICO-SPECT imaging as well as posterior patient detector clearance. A 15%-wide symmetric energy window was used about the 140-keV photopeak from ^{99m}Tc in all studies. The camera used a custom-designed and -built pyramidal collimator support with 14-cm focal length (27,28), which accepts a single and exchangeable pinhole insert shrouded by tungsten shielding. Originally intended to reduce penetration from higher energy γ -rays, the patient-side tungsten shielding secures the exchangeable pinhole inserts yet physically increases the minimum ROR by 4 cm, because it protrudes from the pinhole insert itself (28). Although it may otherwise present a problem for imaging very small volumes because of resolution degradation with the increased distance from the pinhole, this 4-cm distance actually facilitates keeping the relatively large breast phantom entirely within the approximately 90° aperture acceptance angle, and hence within the camera FOV, and also affects the maximum attainable orbital range.

High-Z Pinhole Collimators

The pinhole inserts (Table 1) consisted of tungsten (¹⁸⁴W alloy K1850; Kulite Tungsten Corp., East Rutherford, NJ) and nickel-

plated DU (Los Alamos National Laboratory, Los Alamos, NM) and had knife-edge apertures that varied from 1.0 to 4.0 mm in diameter (28,30). The DU consisted of processed natural uranium from which most of the ²³⁵U had been removed. The aperture angular acceptance systematically decreased from 100° to 85°, with increasing aperture size to match the gamma camera's 40-cm transverse extent for the 14-cm focal length.

The DU pinholes have the highest stopping power of available materials but are slightly radioactive and thus can contribute background counts that can potentially corrupt scans with very low counting rates. These inserts were originally designed for use in high-activity and medium-energy ¹³¹I (364-keV) imaging (30). The background from the 1.0-mm-diameter DU pinhole insert was measured for approximately 12 h with a shielded GeLi detector (model GC2018; Canberra Corp., Meriden, CT). Because of this intrinsic background, however, pinhole inserts of other high-Z, high-density, and nonradioactive materials, such as gold, platinum, or iridium (Table 1), could also potentially be used (31,32) for simultaneously imaging multiple radioisotopes (of different energies) with pinhole apertures.

Phantoms

Various anthropomorphic phantoms filled with aqueous ^{99m}Tc-pertechnetate activity were used in these measurements. A 950-mL volume, rigid breast phantom prototype (single breast) that was 12 cm in the anterior-posterior dimension, with 15-cm major and 13.5-cm minor elliptical diameters, was used in all imaging studies (Fig. 2A).

The fillable left breast contained 2 spherical lesions, 1.0 and 0.6 cm in diameter (0.52 and 0.11 mL, respectively) (ECT/HOL-468/A; Data Spectrum Corp., Hillsborough, NC), with each localized at superior and inferior medial aspects of the breast, parallel to the AOR and 6 cm from the nipple. A radioactively filled elliptical torso phantom (6,650 mL) with myocardial insert (ECT/LUNG/P and ECT/CAR/I; Data Spectrum Corp.) was always used along with the left breast phantom. This combined breast-torso phantom arrangement was tomographically imaged over $\leq 180^\circ$ in an incomplete circular orbit about a pendulous breast reference frame, with the arrangement positioned so that the AOR was located posterior to the center of mass of the breast (10). In contrast but similar to the intended clinical prone application (shown in Fig. 1B), in which camera motion abnormalities encountered during a clinical scan would be unlikely to interfere with or harm the patient, the rigid breast and torso phantoms were

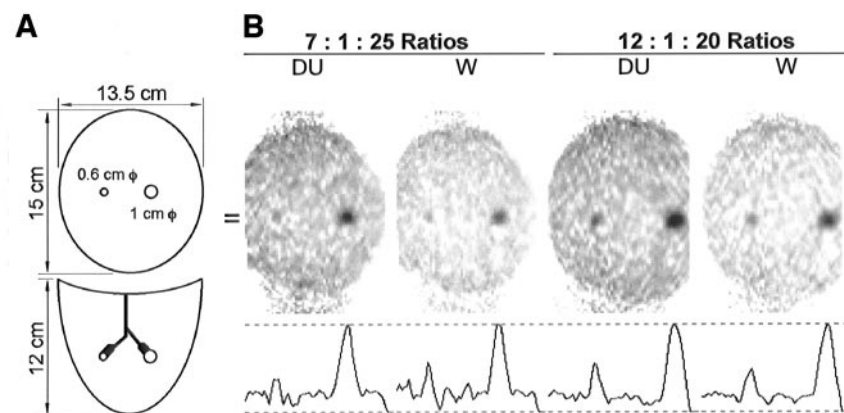


FIGURE 2. (A) Schematic diagram of breast phantom with approximate locations of lesions, with sizes indicated (ϕ = diameter). Coronal view (top) with lesions and sagittal view (bottom) illustrate how lesions were held in place. Materials are made of acrylic. (B) Coronal views of reconstructed images obtained with 3-mm DU and tungsten pinholes at indicated L:B:M activity concentrations. PICO-SPECT data were acquired with trajectory along vertical dimension. Profiles at bottom are obtained from indicated regions through images.

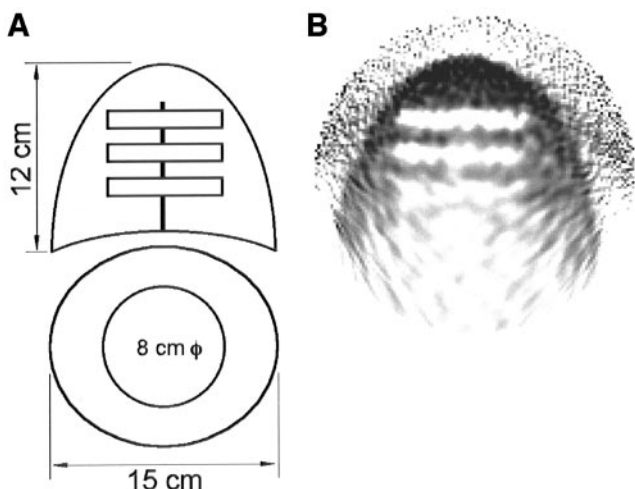


FIGURE 3. (A) Schematic diagram of breast phantom with locations of cold disks of indicated size (ϕ = diameter). Sagittal view (top) with disks held in place and coronal view (bottom) with centered disks. Materials are made of acrylic. (B) Eleven summed sagittal-view slices of reconstructed cold disks inside breast phantom illustrating limited visualization at depth from nipple, located at top of image. Note well-sampled and uniform upper half of figure, proximal to side of pinhole orbit of hemi-ellipsoidal pendant breast imaging frame. Grayscale is adjusted to highlight disks and nonuniform sampling at image bottom.

imaged in a supine orientation in a specialized phantom mounting fixture to facilitate identical repositioning in the studies.

To elucidate limitations of sampling and image uniformity at depth in the breast with PICO-SPECT imaging, 3 uniform acrylic disks, each 1-cm thick \times 8-cm diameter with 1-cm spacing were placed within the breast volume, with the deepest edge extending 8.5 cm from the nipple (Fig. 3A). This insert is modified from a minidisk phantom (ECT/DEF/MP; Data Spectrum Corp.). This phantom arrangement containing 0.76 MBq/mL (20.5 μ Ci/mL) 99m Tc was scanned for 1 h with the 3-mm DU pinhole with 13.4-cm ROR with a 180° rotation for 120 projections (1.5°/projection).

Lesion Concentration Comparisons

For lesion imaging, the center of mass of the breast phantom was located near the camera AOR as described. Two sets of equal length scans (20 min per scan) were performed with different lesion-to-breast and body-to-myocardium (L:B:M) activity concentrations. The first series of acquisitions used L:B:M activity concentration ratios of 12:1:20, where the absolute activity concentration of the lesions was 0.95 MBq/mL (25.6 μ Ci/mL), which is about 4 times what has been clinically observed (1). The second series of experiments used roughly half the first lesion activity concentration in ratios of 7:1:25, where the absolute activity concentration of the lesions was 0.52 MBq/mL (14.2 μ Ci/mL). In both cases, a high myocardial activity concentration was used to determine whether background myocardial activity degraded image quality. This phantom arrangement was scanned with 13.7-cm ROR with a 177° rotation for 118 projections (1.5°/projection) in all cases.

Planar Comparison with PICO-SPECT

A separate series of scans was performed to compare planar pinhole and PICO-SPECT performance with the tungsten aper-

tures at clinical count densities. Because the optimal apertures for planar imaging (pinhole scintimammography) may differ from the optimal aperture for PICO-SPECT, all aperture inserts were measured.

The center of mass of the breast phantom was located near the camera AOR. The 99m Tc activity L:B:M concentration ratios were 11:1:25, and the absolute activity concentration of both lesions was 1.05 MBq/mL (31.0 μ Ci/mL). This activity concentration is approximately 4 times that measured clinically (1), and, to be clinically equivalent, the acquisition times were appropriately shortened by a factor of 4 (5 min vs. 20 min) compared with the lesion concentration scan comparisons described previously. For a given pinhole aperture, PICO-SPECT and single-view planar scan times were identical.

For PICO-SPECT, the breast phantom was scanned with 12.5-cm ROR with a 178.5° rotation for 119 projections (1.5°/projection). Lateral oblique planar pinhole images were also acquired with each pinhole for comparison. For planar imaging, the detector distance to the AOR was 12.5 cm, which was identical to the ROR for the PICO-SPECT scans.

Initial Patient Study

A 52-y-old woman with biopsy-confirmed right breast carcinoma was injected intravenously with 960 MBq (26 mCi) 99m Tc-labeled tetrofosmin (3–5,25) under an Internal Review Board-approved protocol. With ultrasound, the lesion measured 3.7 cm at the largest diameter. Four low-activity, 99m Tc point-source markers were positioned around the right breast: 1 on the nipple and 3 at the periphery (superiorly, inferiorly, and medially). These markers were intended for use for repositioning studies or registration between multimodality (i.e., SPECT and MRI) breast imaging acquisitions. The patient was scanned in the prone position approximately 2 h after injection, lying on the specially designed bed shown in Figure 1. The ROR was 12.7 cm and the 3-mm tungsten pinhole aperture was used. The PICO-SPECT orbit was over a 150° angular range for 100 projections (1.5°/projection) for a total scan time of 20 min. The patient was comfortable for the scan duration, and there was generous clearance of the backside detectors and no physical interference from the pyramidal pinhole support orbiting underneath the bed. With the patient lying prone, the chance of any camera anomalies or physical hindrance that could affect the patient or the scan was considerably reduced. A planar pinhole scan was also acquired for 5 min from a posterior-lateral projection with the same separation distance as ROR for the PICO-SPECT scan.

Image Reconstruction and Analysis

The PICO-SPECT data were reconstructed with pinhole filtered backprojection (FBP) using a 2-dimensional Hann filter ($f_c = 0.75 \times$ Nyquist) unless otherwise indicated. A factor of 2.0 magnification was used in the phantom reconstructions, yielding voxels of 1.78-mm dimension on a side in the $128 \times 64 \times 64$ pixel volumetric images. A smaller magnification factor of 1.5 was used in the patient study reconstruction, yielding voxels of 2.4 mm in each dimension. No attenuation or scatter correction was used.

A set of image data consists of data acquired with 1 L:B:M activity concentration ratio and the various pinhole apertures. The reconstructed phantom images for a given set of data in which both lesions were most clearly visible were rotated into sagittal or coronal views so that both lesion centers were coplanar. All other data for that given set of acquisitions were rotated with identical Euler angles. Profiles were drawn over the images for semiquan-

titative evaluation, and regions of interest (ROIs) were drawn on the larger and smaller lesions and breast background for other semiquantitative information. Values extracted from each ROI were determined by locating the ROI entirely within the visual boundary of the lesion or background region. Within the visual boundary of the lesion, the ROI was moved around incrementally until the smallest variance between all pixel intensities in that ROI was obtained. The mean pixel intensity from that ROI was then used in additional calculations. Three image slices that spanned the center of the coplanar lesions were summed before obtaining values from the ROIs. Breast or background ROIs included a majority of the visible breast, excluding regions between and posterior to the lesions, because the lesion support rods displace activity there. Because of attenuation and scatter, the variance between these central and more peripheral breast background values could be high.

ROI values were obtained from the planar and reconstructed and rotated PICO-SPECT patient data using annular ROIs inside the visible shell-like lesion. Contrast and SNR were determined for the visible lesion. Profiles were drawn across the tumor in various reconstructed coronal and sagittal views along the largest visible dimensions, and the PICO-SPECT dimensions were determined by the measured distance between the half heights of each edge of the lesion along that dimension. This technique was believed to yield a reasonable estimate of the lesion dimensions, because the intrinsically noisy PICO-SPECT data were reconstructed using a filter with high frequency roll-off and with a cutoff below the full Nyquist frequency.

As reported elsewhere (10,15,16,20,21), image contrast was calculated as:

$$\text{Contrast} = \frac{N_{\text{lesion}} - N_{\text{breast}}}{N_{\text{breast}}},$$

and SNR was calculated as:

$$\text{SNR} = \frac{N_{\text{lesion}} - N_{\text{breast}}}{\sigma_{\text{breast}}},$$

where N is the mean pixel intensity in the ROI, and σ is the SD in pixel intensity over the ROI. These metrics were compared for

planar and SPECT data for the various pinhole apertures and various L:B:M phantom activity ratios.

Because of the highly similar calculated values of effective diameter and efficiency (31) along the central ray of the DU and tungsten pinholes at 140 keV (Table 2), the DU and tungsten aperture performances were expected to be quite similar. Indeed, local maxima were measured for both aperture types as a function of aperture size. Thus, quadratic functions, defined as:

$$f(x) = A_1 + (A_2 \times x) + (A_3 \times x^2),$$

where $f(x)$ represents fits to contrast or SNR, and x represents aperture size, were fit to the combined tungsten and DU contrasts and SNRs (i.e., 8 data points combined from 2 pinhole materials and 4 aperture sizes total, instead of 4 points per fit each). From the first derivative of the fits, the locations of the optima within the range of measured aperture sizes were determined.

RESULTS

The GeLi spectrum of the DU collimator measured up to 2 MeV yielded several peaks (Fig. 4A). These low-energy peaks in the GeLi spectra were also evident in the energy spectra measured with the gamma camera (Fig. 4B). The low-energy background peaks occur below but near the 140-keV photopeak in the ^{99m}Tc scatter spectrum and increase in magnitude with smaller pinhole aperture. The peaks may be partly the result of characteristic x-ray fluorescence, which occurs at 115 keV in DU. By subtracting the tungsten energy spectra from the corresponding-sized DU spectra and integrating over a $\pm 7.5\%$ symmetric energy window about the photopeak used to collect the image data, the DU background contribution in the photopeak events was estimated (Table 2). The DU background in the projection images without additional emission events was spatially uniform, yielding decreased image contrast and had an average counting rate for all DU apertures of 62 counts/s over the entire $40 \times 20 \text{ cm}^2$ camera FOV.

TABLE 2
Comparison of Some Calculated Characteristics and Measured Parameters at 140 keV with Pinhole Inserts

Material	Diameter (mm)	Calculated*		Measured	
		Effective diameter (mm)	% Normalized efficiency†	% Sensitivity‡	% Depleted uranium background
Tungsten	1.0	1.0035	6.28	10.8	—
	2.0	2.0032	25.1	28.9	—
	3.0	3.0029	56.3	60.8	—
	4.0	4.0027	100.0	99.2	—
Depleted uranium	1.0	1.0021	6.27	12.3	11.8
	2.0	2.0019	25.0	31.1	7.3
	3.0	3.0017	56.2	59.9	1.5
	4.0	4.0016	99.9	100.0	0.74

*Calculated from data in (31).

†Geometric efficiency calculated along central ray and normalized to 4-mm-diameter tungsten pinhole aperture.

‡Values are normalized to 4-mm depleted uranium pinhole value.

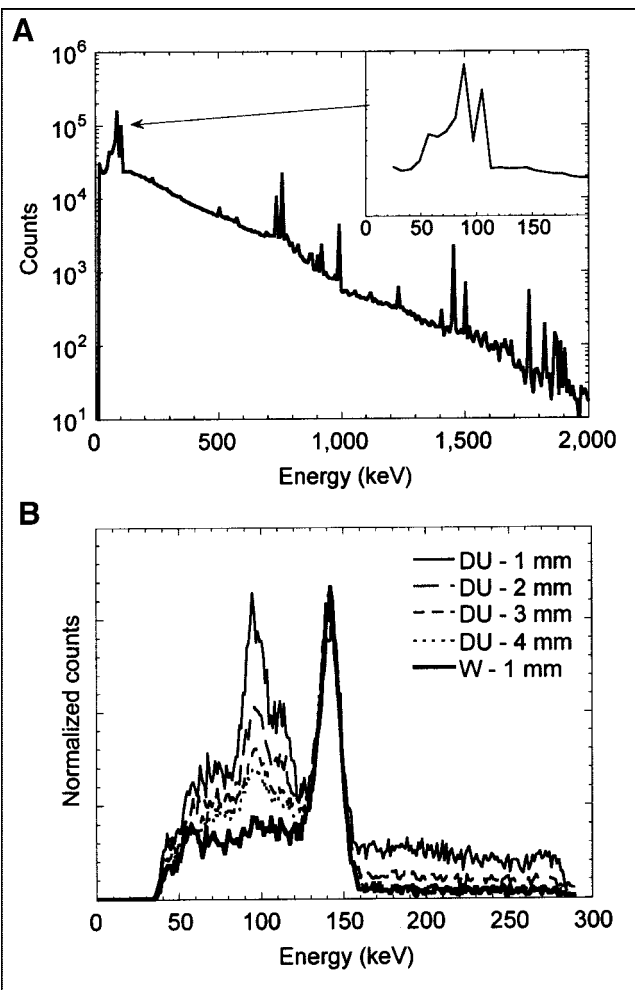


FIGURE 4. (A) GeLi-measured energy response of intrinsic background from 1-mm DU pinhole measured over 12 h. Peaks at arrow tip and inset spectra indicate region of overlap with ^{99m}Tc spectrum. (B) ^{99m}Tc emission spectra measured from fully filled phantoms with gamma camera at fixed location with respect to phantom using DU and tungsten pinholes at indicated sizes. Note additional low- and high-energy components with DU pinholes. Other-diameter tungsten apertures had nearly identical spectra.

As expected, the reconstructed PICO-SPECT image data demonstrated that lesions with lower activity concentrations are more difficult to distinguish than those similarly sized and located lesions with higher activity concentrations (Figs. 2B and 5). For the larger lesion size, measured contrasts formed an extended peak around the 2-mm-diameter aperture, whereas contrast for the smaller lesion increased monotonically with decreasing aperture size (Figs. 5A and 5C). The measured contrast ranges varied from the known 7:1 lesion-to-background ratio (contrast = 6) by factors of 2.8 for the large lesion using a 1-mm-diameter aperture to 11.2 using a 4-mm aperture for the smaller lesion. In general, greater differences were apparent with the larger pinholes and smaller lesions. Similar results were obtained for lesion contrast with the 12:1 activity concen-

tration ratios (contrast = 11), with the measured range of differences from the known activity concentration varying from factors of 2.4 for the large lesion using a 2-mm-diameter aperture to 8.0 using a 4-mm aperture for the smaller lesion. The mean contrast values between tungsten and DU collimator materials were nearly equivalent for the 7:1 and 12:1 concentration measurements. However, there were measured differences ranging from a factor of 1.4 for the 1-mm aperture and 12:1 lesion-to-background ratio to a factor of 2.5 for the 4-mm aperture and 7:1 ratio between contrast values with different lesion sizes. With increasing aperture diameter, improvements in SNRs in factors of 1.6–4.0 from the lowest to highest measured SNR in the set were observed for various lesion sizes and both activity concentrations and pinhole materials (Figs. 5B and 5D). The measured SNRs formed a broad peak between the 2- and 4-mm aperture diameters.

Results for the pinhole planar and reconstructed PICO-SPECT comparison demonstrate that PICO-SPECT images yield improved lesion contrast (Fig. 6). The peak-to-background heights (contrast) in the image profiles of the planar and PICO-SPECT images illustrate clear differences between acquisition approaches. Although data acquired for 1 aperture size with planar and PICO-SPECT imaging were collected for the same times, the collection time between aperture sizes was adjusted to collect approximately 560,000 total counts in both acquisition techniques. These count densities correspond to clinical count densities based on known lesion concentrations (1). In the planar image (Fig. 6A), the activity-filled myocardial insert as well as the acrylic boundary between the breast and torso phantom are clearly visualized; however, visualization of the smaller 0.6-cm lesion is difficult. The myocardial apex is barely

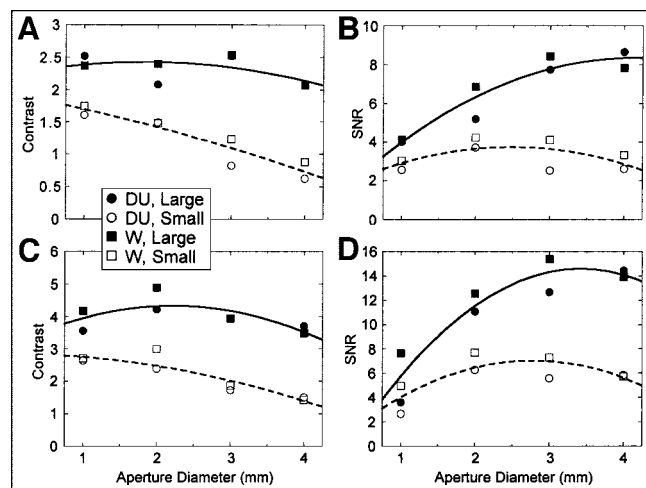


FIGURE 5. Measured PICO-SPECT contrasts for all pinholes with 7:1:25 L:B:M (A) and 12:1:20 L:B:M (C) activity concentration ratios measured for equal times for large (1.0-cm) and small (0.6-cm) lesions. Measured PICO-SPECT SNRs for identical conditions as contrasts, with 7:1:25 L:B:M (B) and 12:1:20 L:B:M (D).

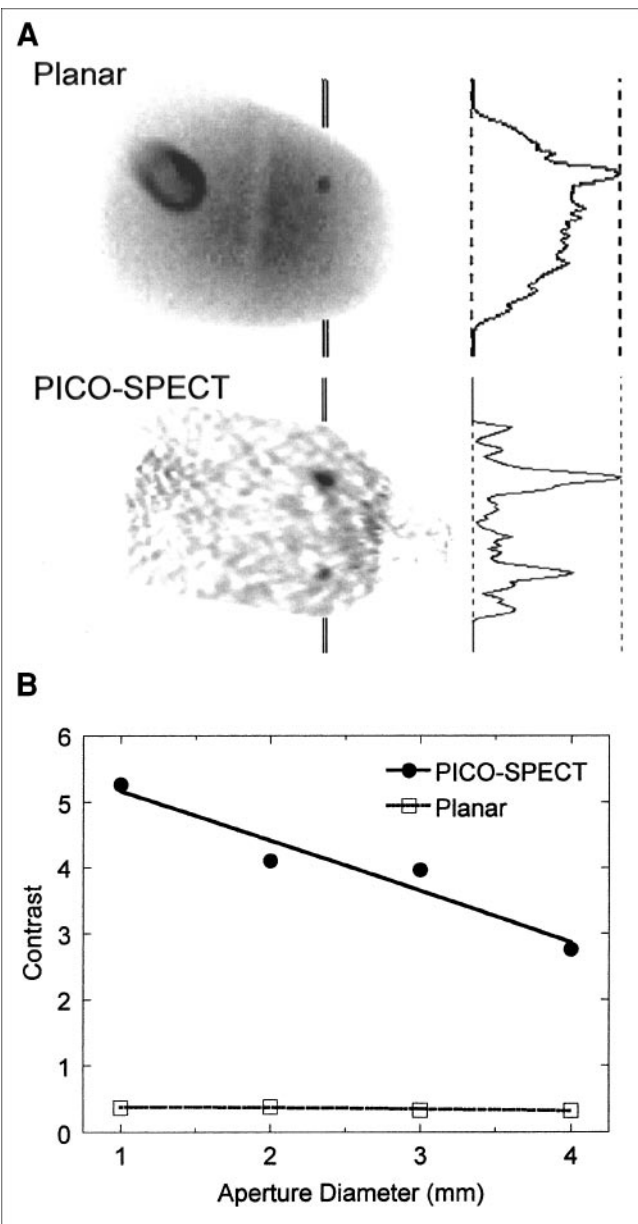


FIGURE 6. (A) Sagittal views of 20-min, clinically equivalent acquired lateral oblique planar (top) and 3 summed slices of FBP-reconstructed PICO-SPECT images (bottom) with their associated profiles at indicated locations through breast phantom containing 2 lesions. Data acquired with 2-mm tungsten pinholes. Breast truncation seen in PICO-SPECT image is result of zoomed FOV, and flattened nipple region (at right) is result of air bubble displacing activity in supine-oriented phantom. (B) Contrast values of large (1-cm) breast lesion measured with planar and PICO-SPECT techniques. All data are from tungsten aperture measurements with 11:1:25 L:B:M activity concentration ratios.

seen at the image left in the reconstructed PICO-SPECT sagittal image (Fig. 6A) because of the zoom used in the reconstruction and because myocardial sampling and distance varied with projection angle, affecting the counts seen from the myocardium as the camera traversed the incomplete circular orbit about the breast.

The reconstruction of the PICO-SPECT acquisition about the cold minidisk phantom inside the radioactively filled breast phantom illustrates both sampling uniformity and depth limitations of this breast imaging approach with a pinhole collimator (Fig. 3B). Under these measurement conditions, sampling is apparently approximately complete to about 7.5 cm from the nipple in the 12-cm-deep breast, as evidenced by the relatively distortion-free recovery of the disks to that depth. The sampling appears to be markedly incomplete past that depth from the nipple, but this still may not preclude adequate hot lesion imaging on nearly uniform backgrounds as evidenced in other approaches (15,16,20).

The images obtained from the initial patient study (Figs. 7 and 8) demonstrate the improvements observed between planar and dedicated PICO-SPECT phantom studies. PICO-SPECT acquisition times were, however, 4 times longer than the planar acquisition. A lesion was clearly seen with both acquisition methods, but the coronal and sagittal slices through the reconstructed PICO-SPECT data revealed decreased intensity in the center of the tumor. The small (approximately 3-mm) distributed point sources can also be seen sporadically (although with some streak artifacts) in the PICO-SPECT images but are not visualized at all in the planar pinhole image. Mean contrast measurements from the sagittal and coronal views, with annular ROIs to account for the center of the lesion with decreased intensity, were measured to be 6.4 times higher with PICO-SPECT than with planar pinhole imaging. The absolute contrast was 11.6, which is 2.5 times greater than the best contrast measured with the phantom-simulated 12:1:20 uptake ratio in the larger tumor with the 3-mm tungsten pinhole.

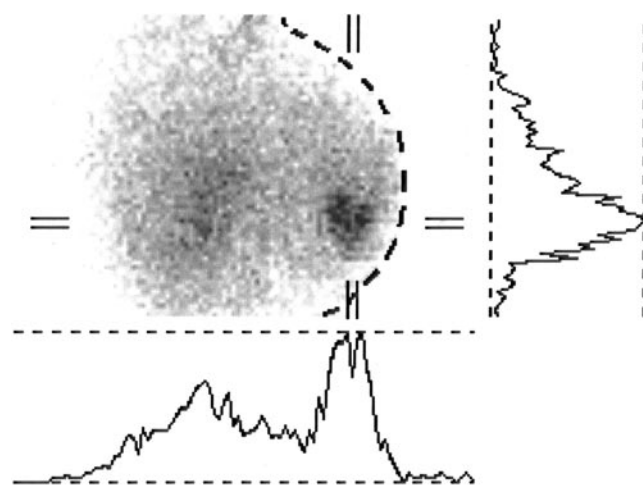


FIGURE 7. Lateral planar pinhole scintimammogram (5-min acquisition) from right pendulous breast of patient with large inferior-anterior-lateral breast lesion. Associated profiles drawn across image at indicated horizontal and vertical locations are shown adjacent to scintimammogram. Dashed curve indicates approximate patient body contour.

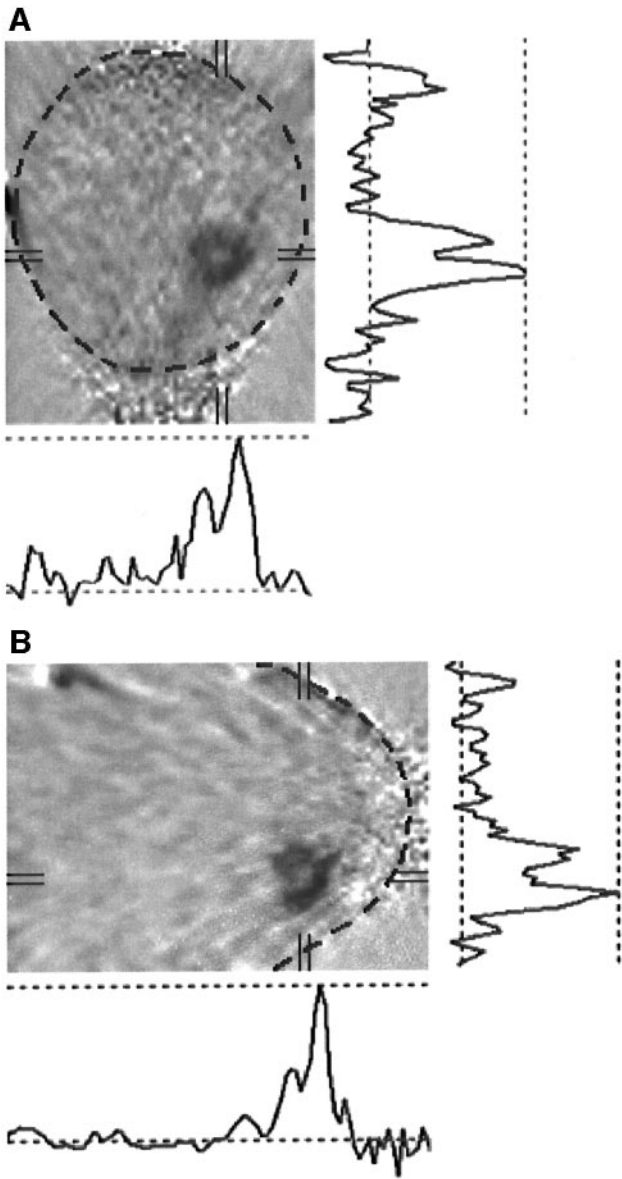


FIGURE 8. (A) Coronal and (B) sagittal views and associated profiles at indicated horizontal and vertical locations of reconstructed slices of same patient in Figure 7, acquired with 20-min PICO-SPECT scan. Dashed curves indicate approximate breast contour. Hot spots near breast periphery indicate signal from point source marker placed around breast base. PICO-SPECT tumor contrast is improved compared with planar image, and different accumulation between periphery and center of patient's lesion is also seen. Grayscale contains negative values resulting from FBP reconstruction and yields gray background outside breast periphery.

DISCUSSION

Several pinhole apertures from 1 to 4 mm and made with 2 different materials were investigated for use with dedicated PICO-SPECT imaging of the breast with ^{99m}Tc compounds. DU was initially investigated as a candidate for higher resolution imaging because of its lower expected edge penetration compared with other collimator materials

at 140 keV, but the results indicated that at this energy and these RORs, both DU and tungsten have similar performance in terms of SNR, contrast, and image quality. Thus, further comparisons of the tungsten apertures were made between the PICO-SPECT approach and planar pinhole imaging, and an optimal tungsten aperture was chosen for an initial clinical patient study.

Because of the nonstandard pinhole aperture material using DU, the intrinsic spectral emission of DU was measured. The presence of the peaks in the DU background spectra (Fig. 4) is caused by trace quantities of fissionable ^{235}U and associated decay products. At medium to high energies (364 to 511 keV), for which these pinholes were originally designed, the continuum of events is most probably caused by β -decay-created bremsstrahlung, with no distinct or predominant transition energies. However, as observed at lower energies (Fig. 4A), there are some peaks, 1 of which may be the result of characteristic x-ray fluorescence that may affect imaging near 140 keV. Characteristic x-ray peaks clearly appear in the gamma camera-measured spectra with DU but not tungsten and, in fact, would otherwise be excluded with photopeak energy windowing.

The intrinsic background from DU was measured to be <12% of the windowed photopeak signal with the smallest aperture and decreased to approximately 5% contribution with the larger 2- to 3-mm apertures. This increased background observed with smaller apertures (Fig. 4B) is related to the relative decrease in pinhole sensitivity for emission events (Table 2) but correspondingly near-constant mass of DU material, hence constant background event rate. Also evident is the high-energy plateau beyond the ^{99m}Tc emission photopeak due to the DU background, and counts in this plateau may partially account for the slightly higher measured sensitivities shown in Table 2.

No spectral degradation was observable with the lower-Z and -density tungsten apertures. Using the tungsten and DU pinhole linear attenuation coefficients to calculate the effective pinhole diameter with Anger's (31) original formula at 140 keV, there should be a <0.1% difference between these pinhole materials for all aperture sizes and specific acceptance angles (Table 2). Thus, tungsten would be a sufficient collimator for high-resolution pinhole imaging at 140 keV without any additional background from the collimator itself.

Slightly higher than expected clinical count scans obtained with each pinhole were also investigated with lesions of different uptake ratios. The coronal views of these reconstructed data (Fig. 2B) demonstrate some truncation of the projection data in the superior-to-inferior (seen from right-to-left) aspects of the reconstructed breast data. This truncation is a potential problem with high-resolution pinhole imaging of the breast if magnification, which may truncate the projections, is used in the reconstruction. More importantly, if the patient's breasts are large and positioning is difficult, truncation is likely. Planar breast imaging (pin-

hole scintimammography) alone can also be limited by partial truncation of the entire breast volume (22). Hence, care must be taken to ensure that the entire breast volume is encompassed throughout the trajectory and that any suspected lesion site is included. With pinhole imaging, there is distortion at the axial extremes of the image because of well-known incomplete sampling there. Ideally, some axial translation could be used to encompass large, pendulous breasts entirely in the FOV. Three-dimensional orbits that use continuous angular rotation with continuous axial bed motion may also be used to more completely sample the entire pendulous breast (18).

Smaller differences were noted between pinholes of different materials than between different aperture sizes (Fig. 5). The trends in lesion SNRs indicate that there are optimal pinhole apertures for different sizes of lesions in this dedicated breast imaging application, and these 2- to 4-mm values correspond with those measured in another tomographic technique (23). In addition, the application of attenuation and scatter compensation may further improve these relative results.

There is a well-defined separation in contrast values of large and small lesions (Figs. 5A and 5C) for various lesion uptakes. The overall results from these measurements are consistent with improvement in contrast as pinhole diameter decreases. For the 12:1:20 ratio and large lesion, the quadratic fit indicated a slight decrease in contrast from 2- to 1-mm-diameter aperture. This could be attributed to measurement noise. Furthermore, the contrast values for both DU and tungsten apertures are very similar for each aperture size, with the results using tungsten pinholes usually slightly better (+9%) than those with DU. This difference indicates that the background contribution from DU (62 counts/s) seems to play an insignificant role in signal degradation compared with the results with nonradioactive tungsten inserts in this application. Because DU is somewhat more difficult to obtain and, more important, to machine to a desired configuration, tungsten apertures would be better for this application.

The individual SNR results for tungsten pinhole collimators with various lesion uptake ratios are on average +20% better than those with DU apertures (Figs. 5B and 5D), indicating that the background from DU may degrade the lesion signal intensity for the same projection image noise. The differences between the mean SNRs measured from smaller and larger lesions with both material types and for both activity concentrations are considerably greater than the differences between SNRs for materials at a fixed aperture diameter. The quadratic parameter estimates for the large lesion yield a near-optimum aperture at 3.8 mm, whereas for the small lesions the near-optimum value is 2.6 mm. Thus, although pinholes with larger apertures would provide better sensitivity, their poorer spatial resolution ability apparently reduces SNR of smaller lesions or lesions with lower radioactive uptake in favor of larger lesions or lesions with greater uptake. These SNR results suggest that

in an effort to detect earlier stage breast cancers, a small aperture (2–3 mm) demonstrates a good trade-off between resolution and sensitivity.

For comparison measurements between planar pinhole imaging and PICO-SPECT, smaller apertures outperformed larger apertures in absolute lesion contrast (Fig. 6B), generally agreeing with the earlier results (Figs. 5A and 5C). (For these measurements, SNR was not calculated; the measurements had nearly identical noise values for a given aperture diameter because the measurements were made for equal times. In this case, the SNR trends track contrast measurements.) Thus, the loss in sensitivity for SPECT with smaller, finer resolution, nonzero-diameter pinholes may be outweighed by the gain in spatial resolution.

Although the planar pinhole studies were not necessarily optimized, a range of aperture sizes was tested. Moreover, these results are corroborated by other recent breast measurements that indicate that pinhole tomographic imaging is superior to pinhole planar breast imaging (23).

Comparisons of the uncompressed breast with PICO-SPECT and planar data indicate that the tomographic acquisitions yield more than a factor of 20 improvements in contrast (Fig. 6B). Comparisons were made only for measured values from the large 1.0-cm lesion, because the small lesion was not observed in all the planar data, especially with the larger, otherwise more sensitive pinholes. For example, calculated contrast values obtained from these small lesion image datasets were large and negative, most likely because of differences measured between 2 small numbers.

Sampling limitations throughout the breast volume were illustrated. The posterior breast side of the most distal disk is 8.5 cm from the nipple. Although blurring is clearly evident at this depth (Fig. 3B), the cold disk up to 7.5 cm can be visualized. Full 360° circular orbit acquisitions perpendicular to the nipple–chest axis (i.e., standard horizontal AOR SPECT) through the breast have demonstrated adequate sampling with artifact reduction (10), but this implementation is not possible with patients or anthropomorphic torso phantoms without torso interference that necessitates very large RORs. Nevertheless, imaging of hot lesions with PICO-SPECT is still possible for expected focal radiotracer uptake and an otherwise uniform background. Insufficient sampling of this general paradigm has not been shown to be problematic in lesion visualization (15,16,20,21). Complete imaging of the axilla, on the other hand, may be considerably more difficult without the use of alternative or additional orbits (18,33,34). One group has successfully used a limited angular acquisition pinhole SPECT centered on the axilla and already obtained improved clinical sensitivity and specificity for lesion identification (25).

The primary reason PICO-SPECT and other SPECT imaging approaches may indeed provide improved SNR and lesion contrast is because of the application-specific nature of the imaging task for dedicated emission mammotomography. The current results imply that smaller breast lesions

or lesions with lower uptake could possibly be detected with small-aperture, high-stopping-power collimators and PICO-SPECT acquisitions.

Images obtained from the initial patient scan illustrated the improved image quality and information content available with dedicated volumetric imaging with PICO-SPECT (Fig. 8). Although the angular acquisition range for the patient was smaller (by approximately 30°) than for the phantom scans because of physical limitations, the reconstructed images yielded additional information about the lesion not available with planar imaging. In this case, increased counts were clearly visualized in the lesion periphery. This patient received preoperative neoadjuvant chemotherapy consisting of doxorubicin and taxol, administered concurrently with hyperthermia. She had a complete pathologic response at the time of surgery.

This initial image set yields information about the viability of this imaging approach by demonstrating a 6-fold contrast improvement over the planar pinhole technique. Resolution limitations resulting from the size of the lesion played a smaller role in this patient scan than in the phantom measurements using smaller solid lesions, and the large lesion size may explain the very large absolute contrast. The tumor widths measured at the profile locations indicated in Figure 8 were all larger (4%–29%) than the largest (3.7-cm) lesion dimension as measured by ultrasound. Because single-photon image resolution degrades with increasing distance, the larger measured size with PICO-SPECT may result from the system resolution fall-off. Overall, 3-dimensional visualization and localization of the lesion, however, were considerably more clear with PICO-SPECT than planar imaging, in addition to the improved contrast.

With pinhole iterative reconstruction techniques modeling spatial resolution, the lesion size and contrast values could be expected to improve. Indeed, iterative reconstruction techniques would minimize image artifacts (9,18,24), and modeling the system response would improve image quality and lead to more accurate quantification overall.

There are, however, some caveats in PICO-SPECT imaging of the breast. Large breasts may not entirely fit into the FOV, and to adequately sample the breast volume without truncation, multiple axial scans may be needed. Three-dimensional orbits designed to satisfy complete sampling conditions may also be important, regardless of breast size (18,33,34). Large RORs may also be required for larger breasts, along with concomitant resolution loss with the increased distance. Scanning the disk phantom within the breast phantom volume demonstrated that there may be sampling insufficiencies at depth for large pendulous breasts. Additional scans with variations in tumor locations throughout the breast still need to be performed. Furthermore, imaging the axilla and tissue near the chest wall could be accomplished with additional static views of those regions.

CONCLUSION

We have demonstrated a new dedicated emission mammomography technique with PICO-SPECT imaging of breast lesions of various sizes and activity concentration ratios, yielding images of small lesions (down to 0.6 cm) with high contrast and SNR. The technique is readily implemented on contemporary clinical SPECT systems equipped with pinhole collimators and appears to be a better technique than conventional planar pinhole scintimammography. Medially located phantom lesions were more easily seen with PICO-SPECT than pinhole scintimammography. However, evaluation with lesions located at several locations throughout the breast, near the anterior chest wall, and axilla are further warranted.

Both DU and tungsten pinhole collimators had nearly equivalent performance for the imaging task at 140-keV imaging of aqueous ^{99m}Tc . Because of easier accessibility to tungsten materials and their fabrication, as well as the lack of additional radioactivity concerns, this high-stopping-power material at 140 keV is recommended along with this imaging technique. Furthermore, it was determined that 2- to 3-mm aperture pinholes provided the best SNR along with fine spatial resolution for smaller lesions and lesions of lower uptake. Although larger diameter apertures performed somewhat better for the larger lesions investigated, smaller apertures are recommended for imaging smaller lesions. Overall, larger apertures yielded lower SNRs for smaller lesion sizes, indicating that the enhanced spatial resolution of the smaller pinholes outweighs the loss in sensitivity.

Image reconstruction with maximum likelihood expectation maximization or other statistical techniques may further improve these results because of the inherent reduction of artifacts, such as from streaking or axial detector blurring, as well as the incorporation of modeling the system response that is possible with those techniques. Further observer studies of optimal aperture size via observer models and receiver operator characteristics may also be warranted to evaluate the efficacy of the technique in a clinical lesion detection task.

ACKNOWLEDGMENTS

The authors thank Caryl Archer and Scott Metzler for technical assistance and useful discussions, Mark Smith for the use of his pinhole reconstruction code, Jörg Peter for the use of his analytical phantom in the figures, Tim Turkington (Duke University) for use of SPECTER version 4.0 for visual display and analysis, and anonymous reviewers for helpful comments. We also thank the Duke University Medical Center Radiopharmacy for providing isotopes, the Section of Nuclear Medicine for use of the Trionix XLT-9 camera, and Nancy Jaszczak of Data Spectrum Corp. for the use of some phantoms. One of the authors (R.J.J.) is an officer and consultant to Data Spectrum Corp. This work was supported by National Institutes of Health/National Cancer Institute grants RO1-CA76006 and RO1-CA33541,

grant RG-99-0305 from the Whitaker Foundation, and Department of Energy grant DE-FG02-96ER62150.

REFERENCES

1. Maublant J, de Latour M, Metstas D, et al. Technetium-99m sestamibi uptake in breast tumor and associated lymph nodes. *J Nucl Med.* 1996;37:922–925.
2. Villanueva-Meyer J, Leonard MH Jr, Briscoe E, et al. Mammoscintigraphy with technetium-99m-sestamibi in suspected breast cancer. *J Nucl Med.* 1996;37:926–930.
3. Mansi L, Rambaldi PF, Procaccini E, et al. Scintimammography with technetium-99m tetrofosmin in the diagnosis of breast cancer and lymph node metastases. *Eur J Nucl Med.* 1996;23:932–939.
4. Rambaldi PF, Mansi L, Procaccini E, di Gregorio F, del Vecchio E. Breast cancer detection with Tc-99m tetrofosmin. *Clin Nucl Med.* 1995;20:703–705.
5. Spanu A, Dettori G, Nuvoli S, et al. ^{99m}Tc -Tetrofosmin SPET in the detection of both primary breast cancer and axillary lymph node metastasis. *Eur J Nucl Med.* 2001;28:1781–1794.
6. Tiling R, Tatsch K, Sommer H, et al. Technetium-99m sestamibi scintimammography for the detection of breast carcinoma: comparison between planar and SPECT imaging. *J Nucl Med.* 1998;39:849–856.
7. Aziz A, Ahmadi R, Ogawa Y, Hayashi K. Tc-99m-MIBI scintimammography: SPECT versus planar imaging. *Cancer Biother Radiopharm.* 1999;14:495–500.
8. Jaszcak RJ, Whitehead FR, Lim CB, Coleman RE. Lesion detection with single photon emission computed tomography (SPECT) compared with conventional imaging. *J Nucl Med.* 1982;23:97–102.
9. Li J, Scarfone C, Jaszcak RJ, Wang H, Coleman RE. Limited angular view MLEM pinhole SPECT for breast tumor detection [abstract]. *J Nucl Med.* 1996;37(suppl):214P.
10. Scarfone C, Jaszcak RJ, Li J, et al. Breast tumor imaging using incomplete orbit pinhole SPET: a phantom study. *Nucl Med Commun.* 1997;18:1077–1086.
11. Wang H, Scarfone C, Greer KL, Coleman RE, Jaszcak RJ. Prone breast tumor imaging using vertical axis-of-rotation (VAOR) SPECT systems: an initial study. *IEEE Trans Nucl Sci.* 1997;44:1271–1276.
12. La Riviere PJ, Pan X, Penney BC. Ideal-observer analysis of lesion detectability in planar, conventional SPECT, and dedicated SPECT scintimammography using effective multi-dimensional smoothing. *IEEE Trans Nucl Sci.* 1998;45:1273–1279.
13. Ivanovic M, Weber DA, Loncaric S. Multi-pinhole collimator optimization for high resolution SPECT imaging. *1997 IEEE Med Imaging Conf Rec.* 1997;2:1097–1101.
14. Pani R, Soluri A, Scaife R, et al. Feasibility study for SPECT mammography based on compact imagers rotating around breast vertical axis. *2000 IEEE Med Imaging Conf Rec.* 2000;3:2136–2139.
15. Pieper BC, Bowsher JE, Tornai MP, Greer KL, Peter J, Jaszcak RJ. Breast tumor imaging using a tiltable head SPECT camera. *IEEE Trans Nucl Sci.* 2001;48:1477–1482.
16. Tornai MP, Bowsher JE, Archer CN, et al. Dedicated breast imaging with an ASET: application specific emission tomograph [abstract]. *J Nucl Med.* 2001;42(suppl):97P.
17. Baird WH, Frey EC, Tsui BMW, Wang Y, Wessell DE. Evaluation of rotating slant-hole SPECT mammography using Monte-Carlo simulation methods. *2001 IEEE Med Imaging Conf Rec.* 2001;3:1331–1334.
18. Bowsher JE, Tornai MP, Metzler SD, Peter J, Jaszcak RJ. SPECT breast imaging using more nearly complete orbits and combined pinhole-parallel-beam collimation. *2001 IEEE Med Imaging Conf Rec.* 2001;3:1328–1330.
19. Majewski S, Kieper D, Curran E, et al. Optimization of dedicated scintimammography procedure using detector prototypes and compressible phantoms. *IEEE Trans Nucl Sci.* 2001;48:822–829.
20. Tornai MP, Bowsher JE, Archer CN, et al. A novel application specific emission tomograph (ASET) for breast imaging. *2001 IEEE Med Imaging Conf Rec.* 2001;2:1161–1165.
21. Metzler SD, Bowsher JE, Tornai MP, Pieper BC, Peter J, Jaszcak RJ. SPECT breast imaging combining horizontal and vertical axes of rotation. *IEEE Trans Nucl Sci.* 2002;49:31–36.
22. Tsui BMW, Wessel DE, Zhao XD, Wang WT, Lewis DP, Frey EC. Imaging characteristics of scintimammography using parallel-hole and pinhole collimators. *IEEE Trans Nucl Sci.* 1998;45:2155–2161.
23. Fahey FH, Grow KL, Weber RL, Harkness BA, Bayram E, Hemler PH. Emission tuned-aperture computed tomography: a novel approach to scintimammography. *J Nucl Med.* 2001;42:1121–1127.
24. Seret A, Defrise M, Blocklet D. 180-degree pinhole SPET with a tilted detector and OS-EM reconstruction: phantom studies and potential clinical applications. *Eur J Nucl Med.* 2001;28:1836–1841.
25. Spanu A, Dettori G, Chiaramida P, et al. The role of ^{99m}Tc -tetrofosmin pinhole-SPECT in breast cancer axillary lymph node staging. *Cancer Biother Radiopharm.* 2000;15:81–91.
26. Gullberg GT, Zeng GL. A cone-beam filtered backprojection reconstruction algorithm for cardiac single photon emission computed tomography. *IEEE Trans Med Imaging.* 1992;11:91–101.
27. Smith MF, Jaszcak RJ. The effect of gamma ray penetration on angle-dependent sensitivity for pinhole collimation in nuclear medicine. *Med Phys.* 1997;24:1701–1709.
28. Tenney CR, Smith MF, Greer KL, Jaszcak RJ. Uranium pinhole collimators for I-131 SPECT imaging. *IEEE Trans Nucl Sci.* 1999;46:1165–1171.
29. National Institute of Standards. Attenuation coefficients. Physics Reference Data. Available at: <http://physics.nist.gov/PhysRefData/XrayMassCoef>. Accessed January 30, 2003.
30. Smith MF, Jaszcak RJ. Lead and tungsten pinhole inserts for I-131 SPECT tumor imaging: experimental measurements and photon transport simulations. *IEEE Trans Nucl Sci.* 1997;44:74–82.
31. Anger H. Radioisotope cameras. In: Hine GJ, ed. *Instrumentation in Nuclear Medicine.* Vol. 1. New York, NY: Academic Press; 1967:516–518.
32. Tenney CR. Gold pinhole collimators for ultra-high resolution Tc-99m small volume SPECT. *2000 IEEE Nucl Sci Symp Conf Rec.* 2000;3:2244–2246.
33. Tuy HK. An inversion formula for cone-beam reconstructions. *SIAM J Appl Math.* 1983;43:546–552.
34. Weng Y, Zeng GL, Gullberg GT. A reconstruction algorithm for helical cone-beam SPECT. *IEEE Trans Nucl Sci.* 1993;40:1092–1101.



SOCIETY OF
NUCLEAR
MEDICINE